



HAL
open science

Quantification of the ferric/ferrous iron ratio in silicates by scanning transmission X-ray microscopy at the Fe L_{2,3} edges

Franck Bourdelle, Karim Benzerara, Olivier Beyssac, Julie Cosmidis, Daniel
R. Neuville, Gordon E. Brown Jr., Erwan Paineau

► To cite this version:

Franck Bourdelle, Karim Benzerara, Olivier Beyssac, Julie Cosmidis, Daniel R. Neuville, et al.. Quantification of the ferric/ferrous iron ratio in silicates by scanning transmission X-ray microscopy at the Fe L_{2,3} edges. *Contributions to Mineralogy and Petrology*, 2013, 166 (2), pp.423-434. 10.1007/s00410-013-0883-4 . hal-02270197

HAL Id: hal-02270197

<https://hal.sorbonne-universite.fr/hal-02270197v1>

Submitted on 23 Aug 2019

HAL is a multi-disciplinary open access archive for the deposit and dissemination of scientific research documents, whether they are published or not. The documents may come from teaching and research institutions in France or abroad, or from public or private research centers.

L'archive ouverte pluridisciplinaire **HAL**, est destinée au dépôt et à la diffusion de documents scientifiques de niveau recherche, publiés ou non, émanant des établissements d'enseignement et de recherche français ou étrangers, des laboratoires publics ou privés.

1 Quantification of the ferric/ferrous iron ratio in silicates by scanning transmission x-ray
2 microscopy at the Fe L_{2,3} edges

3
4 Authors: Franck Bourdelle ^{a,b}, Karim Benzerara ^a, Olivier Beyssac ^a, Julie Cosmidis ^a, Daniel
5 Neuville ^c, Gordon E. Brown Jr ^{d,e}, Erwan Paineau ^{f,g}

6
7 Mailing addresses of the relevant institutions:

8
9 ^a IMPMC, UPMC-CNRS, Case courrier 115, 4 Place Jussieu, 75252 Paris cedex 05, France

10 ^b GeoRessources, Université de Lorraine, UMR 7359 CNRS, 54506 Vandœuvre-lés-Nancy,
11 France

12 ^c Géochimie et Cosmochimie, Institut de Physique du Globe de Paris, Université Paris
13 Diderot, Sorbonne Paris Cité, UMR 7154 CNRS, 1 rue Jussieu 75005 Paris, France

14 ^d Surface & Aqueous Geochemistry Group, Department of Geological and Environmental
15 Sciences, Stanford University, Stanford, CA, 94305-2115, USA

16 ^e SLAC Natl Accelerator Lab, Stanford Synchrotron Radiation Lightsource, Menlo Pk, CA
17 94025 USA

18 ^f Laboratoire de Physique des Solides, Université Paris-Sud, UMR 8502 CNRS, Bâtiment
19 510, 91405 Orsay cedex, France

20 ^g CEA Saclay, IRAMIS, Laboratoire Interdisciplinaire sur l'Organisation Nanométrique et
21 Supramoléculaire, 91191 Gif-sur-Yvette cedex, France

22
23 Corresponding authors:

24 1. Franck Bourdelle

25 Present mailing address: GeoRessources, Université de Lorraine, UMR 7359 CNRS, 54506
26 Vandœuvre-lés-Nancy, France

27 E-mail address: franck.bourdelle@gmail.com

28 Phone number: + 33 (0)3 83 68 47 28

29
30 2. Karim Benzerara

31 Mailing address: IMPMC, UPMC-CNRS, Case courrier 115, 4 Place Jussieu, 75252 Paris
32 cedex 05, France

33 E-mail address: Karim.Benzerara@impmc.upmc.fr

34 Phone number: + 33 (0)1 44 27 75 42

35

36 **Abstract**

37

38 Estimation of $\text{Fe}^{3+}/\Sigma\text{Fe}$ ratios in materials at the submicrometer scale has been a long-standing
39 challenge in the Earth and environmental sciences because of the usefulness of this ratio in
40 estimating redox conditions as well as for geothermometry. To date, few quantitative methods
41 with submicrometric resolution have been developed for this purpose, and most of them have
42 used electron energy-loss spectroscopy (EELS) carried out in the UHV environment of a
43 transmission electron microscope (TEM). Scanning transmission x-ray microscopy (STXM)
44 is a relatively new technique complementary to TEM and is increasingly being used in the
45 Earth sciences. Here, we detail an analytical procedure to quantify the $\text{Fe}^{3+}/\Sigma\text{Fe}$ ratio in
46 silicates using Fe $L_{2,3}$ -edge x-ray absorption near edge structure (XANES) spectra obtained by
47 STXM, and we discuss its advantages and limitations. Two different methods for retrieving
48 $\text{Fe}^{3+}/\Sigma\text{Fe}$ ratios from XANES spectra are calibrated using reference samples with known Fe^{3+}
49 content by independent approaches. The first method uses the intensity ratio of the two major
50 peaks at the L_3 -edge. This method allows mapping of $\text{Fe}^{3+}/\Sigma\text{Fe}$ ratios at a spatial scale better
51 than 50 nm by the acquisition of 5 images only. The second method employs a 2-eV-wide
52 integration window centred on the L_2 maximum for Fe^{3+} , which is compared to the total
53 integral intensity of the Fe L_2 -edge. These two approaches are applied to metapelites from the
54 Glarus massif (Switzerland), containing micrometer-sized chlorite and illite grains and
55 prepared as ultrathin foils by Focused Ion Beam milling. Nanometre-scale mapping of iron
56 redox in these samples is presented, and shows evidence of compositional zonation. The
57 existence of such zonation has crucial implications for geothermometry and illustrates the
58 importance of being able to measure $\text{Fe}^{3+}/\Sigma\text{Fe}$ ratios at the submicrometer scale in geological
59 samples.

60

61 Keywords: ferric/ferrous iron, STXM, XANES spectroscopy, $L_{2,3}$ -edge, redox mapping,
62 silicate.

63

64 **Introduction**

65

66 Determination of the redox state of iron and its spatial variations in sediments and
67 rocks is of critical importance in both geosciences and environmental sciences, because of the
68 need to understand redox state during their deposition or formation as well as subsequent

69 changes in redox state due to weathering and other processes (e.g., de Andrade et al. 2006;
70 Muñoz et al. 2006; Bernard et al. 2010; Benzerara et al. 2011; Bolfan-Casanova et al. 2012;
71 Stagno et al. 2013). In addition, quantification of $\text{Fe}^{3+}/\Sigma\text{Fe}$ ratios can yield a better insight into
72 the chemistry of complex geological materials (e.g., Muñoz et al. 2006), or a better estimation
73 of P - T conditions by geothermobarometers, when variations of the Fe^{3+} content within the
74 crystals are taken into account (e.g., Schmid et al. 2003; de Andrade et al. 2006; Bourdelle et
75 al. 2013a). Therefore, assessment of the $\text{Fe}^{3+}/\Sigma\text{Fe}$ ratio in minerals is an important and long-
76 standing issue. Different techniques have been used extensively in the past for this purpose,
77 including electron microprobe analysis (EMPA, e.g., Fialin et al. 2004), Mössbauer
78 spectroscopy (e.g., Beaufort et al. 1992) x-ray photoelectron spectroscopy (XPS, e.g.,
79 Raeburn et al. 1997a, b), or x-ray absorption near edge structure (XANES) spectroscopy at
80 the K edge (e.g., Waychunas et al. 1983; Bajt et al. 1994; Wilke et al. 2001, 2009; Berry et al.
81 2003, 2010). However, none of these methods provides spatial resolution at the few
82 nanometers scale, which is particularly useful for studying chemical zonation patterns
83 observed in low-temperature systems. Several studies (e.g., van Aken and Liebscher, 2002)
84 have shown that electron energy-loss spectroscopy (EELS) carried out in a transmission
85 electron microscope (TEM) is a powerful method for determining the redox state of iron at a
86 submicrometer resolution. However it sometimes induces severe beam damage effects, such
87 as electron beam-induced oxidation of iron (Lauterbach et al. 2000; Garvie et al. 2004), the
88 effect of which can be corrected by measuring the signal as a function of time. Alternatively,
89 XANES spectroscopy at the Fe $L_{2,3}$ edges carried out with a scanning transmission x-ray
90 microscope (STXM) has been increasingly used in the Earth and environmental sciences to
91 infer qualitatively $\text{Fe}^{3+}/\Sigma\text{Fe}$ ratios in geological and environmental samples at a spatial
92 resolution of ~ 50 -nm (e.g., Wasinger et al. 2003; Carlut et al. 2010; Lam et al. 2010; de Groot
93 et al. 2010; Miot et al. 2011; Boulard et al. 2012). This technique has several advantages such
94 as offering a high energy resolution (better than 0.1 eV at existing synchrotron facilities) and
95 the possibility of maintaining samples under anoxic conditions before and during the
96 measurement (e.g., Miot et al. 2009). However, no calibration of the STXM-based Fe $L_{2,3}$ -
97 edge XANES approach has yet been carried out, whereas calibration of the EELS approach
98 was quantified by van Aken and Liebscher (2002). Fe $L_{2,3}$ -edges result from $2p \rightarrow 3d$
99 electronic transitions, as shown by Wasinger et al. (2003). These authors described in detail
100 the physical basis of Fe L edges, and showed that information about iron valency can be
101 retrieved from XANES spectra by a multiplet calculation approach (e.g., van der Laan and
102 Kirkman, 1992; Cressey et al. 1993). This approach is difficult to apply when dealing with

103 mineral phases for which we do not know the structure. Alternatively, fitting of XANES
104 spectra with a linear combination of normalized reference spectra has been performed by Miot
105 et al. (2009), but requires appropriate Fe^{2+} and Fe^{3+} end-member reference compounds with
106 Fe in the same local coordination environment as in the sample of interest. Van Aken and
107 Liebscher (2002) have shown the possibility of a third approach that they calibrated for EELS
108 and which uses an empirical correlation between $\text{Fe}^{3+}/\Sigma\text{Fe}$ ratios and a parameter (i.e.,
109 modified integral white-line intensity ratio) which is directly retrieved from EELS spectra at
110 the Fe $L_{2,3}$ edges, and is independent of the coordination environment of Fe to a the first-order
111 approximation.

112 Here we propose an empirical approach similar to that of van Aken and Liebscher
113 (2002) to calibrate the correlation between $\text{Fe}^{3+}/\Sigma\text{Fe}$ ratio and some parameters extracted from
114 the STXM-derived XANES Fe $L_{2,3}$ -edge spectra of reference silicate glasses and
115 phyllosilicates. Two empirical calibrations are proposed, both of which offer a compromise
116 between speed and accuracy of the analytical measurement. An application of this approach to
117 ultra-thin sections of natural chlorites and micas is presented to illustrate the methodology and
118 to further assess the range of applicability of this calibration for STXM.

119

120 **Materials and Methods**

121

122 *Reference samples*

123

124 The samples used in this study were reference synthetic silicate glasses, natural
125 phyllosilicates and fayalite, prepared as powders or ultra-thin sections cut by Focused Ion
126 Beam (FIB) milling. The bulk chemical compositions of the five synthetic glasses were
127 previously determined by Magnien et al. (2004). All samples are composed of similar
128 proportions of Si, Mg, Ca, Na and Fe. The SiO_2 and FeO contents are ~52 wt% and ~13 wt%,
129 respectively. Bulk $\text{Fe}^{3+}/\Sigma\text{Fe}$ ratios were determined by wet chemistry, Mössbauer
130 spectroscopy and EMPA and range from 0.09 to 0.94 (Table 1; Magnien et al. 2004). For
131 STXM-XANES analyses, we ground these samples in deaerated and deionized water, inside
132 an anoxic glovebox ($p(\text{O}_2) < 50$ ppm) to avoid oxidation during sample preparation.

133 The phyllosilicate samples have 2:1 and 2:1:1 structures and their bulk compositions
134 were investigated previously by Joswig et al. (1986), Keeling et al. (2000), Shingaro et al.
135 (2005), Rigault et al. (2010), and in the present study by EMP analyses. Total Fe contents
136 vary significantly between samples and bulk $\text{Fe}^{3+}/\Sigma\text{Fe}$ ratios ranging between 0.03 and 1.0

137 were measured by Mössbauer spectroscopy, EXAFS (extended x-ray absorption fine
138 structure) and/or EELS (Table 1). In addition, a fayalite sample was used as a pure Fe²⁺
139 reference. For STXM-XANES analyses, some samples (smectite Nau-2, chlorites GAB 42,
140 VNI 92, VNI 114, fayalite) were prepared by grinding in deaerated and deionized water in an
141 anoxic glovebox (p(O₂) < 50 ppm). Other samples (clintonite, chlorite ‘prochlorite’, chlorite
142 Ch1, Ti-mica) were prepared by FIB milling.

143 Samples transparent to soft x-rays are needed to measure XANES spectra in the
144 transmission mode of STXM, therefore requiring the preparation of thin samples. FIB foils
145 were cut with a FEI Model 200 TEM FIB system at University Aix-Marseille using the
146 protocol detailed by Heaney et al. (2001). A 30 kV Ga⁺ beam operating at ~20 nA excavated
147 the sample to a depth of 5 µm. The sample foil was then further thinned to ~80-100 nm at
148 lower beam voltage (5 kV) and current (~100 pA), in order to remove the layer damaged by
149 high-energy ions (Bourdelle et al. 2012).

150

151 *Glarus field samples*

152

153 The Glarus Alps (Switzerland) belongs to the Helvetic zone of the northern margin of
154 the Central Alps, and was affected by low-grade metamorphism. Details about the location
155 and composition of the samples analyzed by STXM in the present study are provided in
156 Lahfid et al. (2010). The selected rock samples are metapelites, more or less clayey or sandy
157 marls, with various proportions of quartz, calcite, and clay minerals. Three samples (noted
158 Glarus GL07 13, 16, and 20, as in Lahfid et al. 2010), containing chlorites and K-deficient
159 micas, were milled by FIB. The compositions of the chlorites and micas were obtained on the
160 FIB foils by analytical electron microscopy analyses described elsewhere (Bourdelle et al.
161 2012).

162

163 *XANES spectroscopy*

164

165 Part of the STXM analyses were performed at the Advanced Light Source (ALS)
166 (Lawrence Berkeley National Laboratory) on branch line 11.0.2.2 following the procedures
167 described in Miot et al. (2009). The ALS storage ring was operated at 1.9 GeV and 500 mA
168 current in a top-up mode. More details on the branch line 11.0.2.2 and beam characteristics
169 are given by Bluhm et al. (2009). Stacks of images were obtained by scanning the sample in

170 the x–y directions of selected sample areas over the 690–730 eV energy range (Fe L_{2,3}-edge)
171 using an energy increment of 0.789 eV between 690 and 705 eV, 0.10 eV in the 705–713 eV
172 energy range, 0.19 eV in the 713–719 eV energy range, 0.155 eV in the 719–726 eV energy
173 range, and 0.475 eV in the 726–730 eV energy range. The dwell time per pixel and energy
174 point was 1.3 ms.

175 Some data (chlorite Ch1, chlorite ‘prochlorite’ and Ti-mica) were acquired on the
176 Pollux beamline at the Swiss Light Source (SLS, Villigen, Switzerland). The SLS synchrotron
177 storage ring was operated at 2.4 GeV and 300 mA current in a top-up mode during data
178 collection, and the characteristics of the beamline are detailed by Raabe et al. (2008). Stacks
179 were obtained over the 690–730 eV energy range (Fe L_{2,3}-edge) using an energy increment of
180 0.667 eV between 690 and 700 eV, 0.15 eV in the 700–715 eV energy range, 0.40 eV in the
181 715–727 eV energy ranges, and 0.89 eV in the 727–730 eV energy range. The dwell time per
182 pixel and energy point was 3.5 ms.

183 At both the ALS and the SLS, focus was achieved systematically for each sample, and
184 precision in the determination of the focus position was better than the focus depth. Image
185 stacks were aligned and XANES spectra were derived from areas of interest using the
186 aXis2000 software (Hitchcock, 2012). Potential beam damage caused by the incident photon
187 beam was assessed by monitoring spectral changes at the Fe L_{2,3}-edge with increasing dwell
188 times up to a hundred milliseconds (10, 50, and 100 ms).

189

190 *Spectra processing*

191

192 Energy calibration was performed using the gaseous neon 1s → 3p electronic
193 transition at 867.3 eV. As explained in Figure 1, the processing of spectra consisted of two
194 steps. First, the contribution of lower energy absorption edges (i.e., background) was removed
195 so that in the end, the pre-edge region is set to 0 optical density (noted OD) with a slope of
196 zero. For that purpose, a “linear background” correction was applied to the spectrum. Second,
197 the two edge steps resulting from transitions to unoccupied states in the continuum were
198 subtracted using the following double arctan function (Chen et al. 1995; van Aken and
199 Liebscher, 2002; Brotton et al. 2007):

200

$$201 \quad f(\Delta E) = \frac{h_1}{\pi} \left(\arctan \left[\frac{\pi}{w_1} (\Delta E - E_1) \right] + \frac{\pi}{2} \right) + \frac{h_2}{\pi} \left(\arctan \left[\frac{\pi}{w_2} (\Delta E - E_2) \right] + \frac{\pi}{2} \right) \quad (1)$$

202

203 where h_1 and h_2 are the step heights of the two arctan functions, w_1 and w_2 are fixed peak
204 widths, and E_1 and E_2 are the positions of the inflection points resulting in an energy near the
205 edge onset. Here, w_1 and w_2 are fixed to 1 eV (Fig. 1). Broton et al. (2007) proposed setting
206 the function slope w at 5 eV, to account for the slow onset of the continuum. They argued that
207 a value smaller than 5 eV could induce spurious structures in the background-corrected
208 spectrum. We observed that values of $w = 1$ eV or $w = 5$ eV provided similar results.

209

210 **Results and Discussion**

211

212 *Evolution of Fe L_{2,3}-edge XANES spectra with changes in Fe³⁺/ΣFe*

213

214 XANES spectra at the Fe L_{2,3}-edges of the reference phyllosilicates, fayalite and five
215 Fe-bearing silicate glasses, corrected for continuum absorption, are shown in Figure 2, and the
216 positions of major peaks are summarized in Table 1. These spectra are qualitatively similar to
217 those described in several previous studies and were obtained using different analytical
218 techniques (e.g., Crocombette et al. 1995; Heijboer et al. 2003; van Aken and Liebscher,
219 2002). Four major Fe L_{2,3}-edge XANES peaks are present in all samples. The two major
220 peaks on the L₃ edge are noted as “L₃-a” and “L₃-b”, and similarly, the major peaks on the L₂
221 edge are noted as “L₂-a” and “L₂-b”. For all samples examined, the measured separations of
222 the Fe L₃ and L₂ maxima, due to spin-orbit splitting (van Aken and Liebscher, 2002), are 12.9
223 ± 0.4 eV and 14.2 ± 1.4 eV for peaks a and b, respectively in agreement with previous EELS
224 and XANES studies (e.g., de Smit et al. 2008; de Groot et al. 2010). However, although most
225 of the spectra show a single asymmetrical L₃-a peak, some of them (i.e., VNI 92, VNI 114
226 and GAB 42, fayalite) display an “L₃-a” split into two peaks. In addition, these specific
227 spectra show additional peaks on the L₃-a side at ~706.3 and ~706.8 eV. According to
228 Wasinger et al. (2003), the presence of these minor peaks may be due to a specific atomic
229 environment and/or orbital co-valency of iron in these mineral phases. Similarly, several
230 minor peaks can be observed at around 719.8 eV on the L₂-edge for several samples (VNI 92,
231 VNI 114, GAB 42, PyrNa 17R, fayalite).

232

233 The relative intensities of the different major peaks vary depending on the Fe³⁺/ΣFe
234 ratio (Figure 2). With increasing Fe³⁺/ΣFe ratios, the relative intensity of the L₃-a peak
235 decreases compared to that of the L₃-b peak; L₃-a is more intense than L₃-b in the XANES
spectrum of the VNI 92 sample (Fe³⁺/ΣFe = 0.35), whereas the opposite is observed for PyrNa

236 5R ($Fe^{3+}/\Sigma Fe = 0.61$). Likewise, the relative intensity of L₂-a progressively decreases whereas
 237 that of L₂-b increases as $Fe^{3+}/\Sigma Fe$ increases. The energy position of L₂-b changes very little
 238 between the samples, whereas peaks L₃-a and L₂-a shift slightly towards higher energies when
 239 $Fe^{3+}/\Sigma Fe$ increases.

240

241 *Quantification of $Fe^{3+}/\Sigma Fe$ from XANES Fe L_{2,3}-edge intensity ratios*

242

243 As documented in Figure 2, the main variations in the XANES spectra of reference
 244 samples with varying $Fe^{3+}/\Sigma Fe$ ratios involve the L₃-b/L₃-a intensity ratio. More precisely, the
 245 L₃-b/L₃-a intensity ratio is linearly correlated with $Fe^{3+}/\Sigma Fe$ ratio with only a little scatter (R^2
 246 = 0.96) for both the phyllosilicates and silicate glasses (Figure 3). The correlation is described
 247 by equation (2):

248

$$249 \frac{Fe^{3+}}{\sum Fe} = \frac{R_{L_3} - 0.1867}{0.01991} \quad \text{with} \quad R_{L_3} = \frac{I(L_3 - b)}{I(L_3 - a)} \quad (2)$$

250

251 This approach requires only five XANES images to map $Fe^{3+}/\Sigma Fe$ (see Figure 4 and below):
 252 two images in the pre-edge (needed to apply the “linear background correction” at each pixel
 253 of the image), one at 708.7 eV to quantify the L₃-a peak, one at 710.25 eV to quantify the L₃-
 254 b peak, and one at 718 eV, to remove the edge step of the arctan function. Finally, the ratio of
 255 the resulting 708.7 and 710.25 eV images can be used to determine the R_{L_3} parameter at each
 256 pixel of the image.

257 This calibration is useful but has some limitations. The L₃ peaks, which are much
 258 more intense than the L₂ peaks, are more susceptible to absorption saturation (see Hanhan et
 259 al. 2009, where saturation effects are described for Ca 2p edge spectra). This phenomenon
 260 occurs when the sample is too thick and/or highly concentrated in Fe implying that few
 261 photons are transmitted. This may trigger a non-linear response of the detection and an
 262 artifactual modification of the relative peak heights. The use of a spectral parameter correlated
 263 with $Fe^{3+}/\Sigma Fe$ based on the less absorbing L₂-edge may provide in this case an interesting way
 264 of circumventing absorption saturation issues encountered with the L₃-edge.

265 Figure 2 shows that an increase of $Fe^{3+}/\Sigma Fe$ is associated with a decrease of the
 266 intensity of L₂-a. Figure 5 shows the correlation between $Fe^{3+}/\Sigma Fe$ and R_{L_2} , a ratio that reflects
 267 the importance of L₂-b relative to the total L₂. Similar to the modified intensity defined by van
 268 Aken and Liebscher (2002), the L₂-b contribution is computed as an integration window of 2

269 eV width centred around the maximum L₂-b intensity; the ratio R_{L_2} is calculated from this
270 modified L₂-b intensity and the total integral intensity of L₂-edge. The correlation is high (R^2
271 = 0.97), and is described by equation (3):

$$273 \quad \frac{Fe^{3+}}{\sum Fe} = \frac{R_{L_2} - 0.1476}{0.00297} \quad \text{with} \quad R_{L_2} = \frac{I(L_2 - b)_{\text{mod}}}{A(L_2)_{\text{total}}} \quad (3)$$

274
275 This approach requires the acquisition of a complete stack of images (i.e., as many images as
276 energy points are required to obtain a complete spectrum with a given spectral resolution)
277 between 715 and 730 eV, to cover the entire L₂-edge, and to calculate the double arctan
278 function (equation (1)). As a consequence, the acquisition time required for this method is
279 longer than for the L₃-b/L₃-a intensity ratio method (e.g. 30-40 min *versus* 5-10 min for an
280 area of 150 by 150 pixels). However, this second method seems to be more accurate,
281 especially because (1) the calibration data are less scattered (Fig. 5 *versus* Fig. 3) and (2) the
282 intensity integration improves the signal-to-noise ratio. Several other methods of calibration
283 have been tested, sometimes giving equation with a high correlation (with a R^2 up to 0.95),
284 but the two methods proposed here seem to be a good trade-off between $Fe^{3+}/\sum Fe$ estimation
285 accuracy, acquisition time and ease of use.

287 *Assessment of saturation and beam damage effects*

289 When particles are sufficiently thin, the intensity of each spectral feature changes
290 linearly with thickness. However, Hanhan et al. (2009) showed that in the case of samples that
291 are too thick, one can observe distortions of the Ca 2p spectrum due to a saturation effects.
292 These observations led the authors of that study to set a maximum peak intensity, which
293 should not be exceeded to avoid saturation phenomena.

294 Similarly, we determined the maximum peak intensity below which the Fe L₂₃ spectra
295 are undistorted and vary linearly. For this purpose, a powder of the smectite Nau-2 sample
296 with grains of various sizes was analyzed by STXM. Figure 6 plots the difference between the
297 intensities at 710.35 (L₃-b) and 723.54 eV (L₂-b) (corrected from the pre-edge intensity) vs.
298 the intensity at 710.35 eV (L₃-b, i.e., the peak of maximum intensity for Nau-2, hence the
299 most susceptible to saturation) for each pixel of the stack of images (i.e., a total of 6336
300 pixels). The difference between L₃-b and L₂-b intensities increases linearly when L₃-b
301 intensity is lower than ~1.5 OD. Once the L₃-b intensity exceeds 1.5 OD, the L₃-b – L₂-b

302 difference increases more slowly than L₃-b, underlining (i) the distortion of the spectra for the
303 considered pixels, and (ii) the faster increase of L₂-b intensity compared to that of L₃-b with
304 increasing sample thickness. All the data presented in this study were therefore collected from
305 areas presenting a L₃ peak intensity lower than 1.5 OD.

306 The spectrum may be also influenced by the crystal orientation relative to the direction
307 of polarization of the x-ray beam, a process called linear dichroism. Therefore several
308 XANES spectra were measured on the same part of a FIB foil after sequential rotation of the
309 linear polarisation (see Benzerara et al., 2011 for details on the procedure). The variation of
310 resulting Fe³⁺/ΣFe estimates is negligible, showing that sample orientation does not affect the
311 Fe³⁺ quantification.

312 Beam damage can also potentially alter assessment of the Fe³⁺/ΣFe ratio. Here, beam
313 damage was evaluated by monitoring spectral changes at the Fe L_{2,3}-edge with increasing
314 dwell times from 10 up to 100 milliseconds. Figure 7 shows that Fe³⁺/ΣFe ratios derived from
315 XANES spectra are only slightly affected by increasing dwell time. In particular, no
316 significant change was observed for typical dwell times used during routine analyses of the
317 samples (i.e., ~1.3 and 3.5 ms per energy- and image-point for ALS and SLS synchrotrons,
318 respectively).

319

320 *Application to a geological case: chlorites and micas from Glarus (Central Alps, Switzerland)*

321

322 To go further, we have applied the methods proposed here on micrometer-sized
323 chlorite and mica/illite-like grains sampled in the Glarus area of Switzerland and cut by FIB-
324 milling. The temperatures of chlorite formation were calculated from analytical electron
325 microscopy (AEM) chemical analyses, based on the thermometer by Bourdelle et al. (2013b),
326 which does not require Fe³⁺/ΣFe input, and the thermometer by Inoue et al. (2009), which
327 needs a previous estimation of Fe³⁺ content. The Fe³⁺/ΣFe ratios were estimated for each FIB
328 foil by XANES from equations (2) and (3). The results are given in Figure 8 and Table 2.

329 From images converted to optical density units taken at 708.7 eV, we can easily
330 distinguish Fe-rich and Fe-poor minerals: chlorites appear as light grey and represent the Fe-
331 rich phase, whereas micas are dark, i.e., Fe-poor. XANES spectra, acquired along the mica-
332 chlorite contacts show that the Fe³⁺/ΣFe ratio is higher in illite than in chlorite: the Fe³⁺/ΣFe
333 ratios estimated by equation (3) range from 22.3% to 27.9% in chlorite, whereas these ratios
334 vary between 30 and 65.5% in illite-like phase. Equation (2) provides consistent estimations,
335 suggesting that both calibrations are reliable. This analysis shows that K-deficient micas can

336 contain a high proportion of ferric iron (e.g. samples 13 and 20). Despite the relatively high
337 $\text{Fe}^{3+}/\Sigma\text{Fe}$ ratio in some illite-like crystals, the total Fe^{3+} content remains higher in chlorite.

338 Figure 8 also shows the variations of $\text{Fe}^{3+}/\Sigma\text{Fe}$ ratios vs. the temperature of formation,
339 which was estimated by chlorite thermometry (Table 2). In this respect, $\text{Fe}^{3+}/\Sigma\text{Fe}$ ratio
340 increases slightly in chlorites with increasing temperature, whereas this ratio decreases in K-
341 deficient micas. It should be noted that, contrarily to the Bourdelle et al. (2013b) model, some
342 geothermometers based on thermodynamic models for chlorite (e.g., Inoue et al. 2009),
343 require prior determination of the $\text{Fe}^{3+}/\Sigma\text{Fe}$ ratio. When this value is not known, it is set to
344 zero as the default in these types of models. Interestingly, the comparison of results provided
345 by different thermometers in Table 2 shows that the Inoue and Bourdelle geothermometers
346 yield very different temperature results (differences of up to 76°C) when $\text{Fe}^{3+}/\Sigma\text{Fe}$ ratio is not
347 known. In contrast, taking into account the $\text{Fe}^{3+}/\Sigma\text{Fe}$, the two thermometers provide more
348 similar temperatures estimates (a maximum difference of less than 28°C , i.e., within the
349 uncertainty of the thermometers), showing the cross-check validity of the $\text{Fe}^{3+}/\Sigma\text{Fe}$
350 estimation. A variation of the $\text{Fe}^{3+}/\Sigma\text{Fe}$ ratio from 0 to $\sim 23\%$ in chlorites implies a decrease in
351 the temperatures calculated by the Inoue model of 20, 40, and 46°C depending on the sample.

352 Figure 9 displays an example of $\text{Fe}^{3+}/\Sigma\text{Fe}$ mapping at the nanometer-scale derived
353 from images at 706, 708.7, 710.25, and 718 eV using Eq. (2) (see Figure 4). The analysis was
354 carried out on the Glarus GL07 20 FIB foil. The scanned area measures 3.3×3.5 micrometers
355 with a pixel size of 88 nm x 88 nm. The analysis of the illite-chlorite contacts by AEM
356 showed that they are approximately perpendicular to the FIB foil surface, i.e., there is only a
357 little overlap between the two minerals at their contact. The spatial averaging effect of the x-
358 ray beam over the pixel size (i.e., 88 nm) sets the limit of the minimum distance over which
359 illite-chlorite contacts can be discriminated. Beyond this distance, the intracrystalline
360 variation of the $\text{Fe}^{3+}/\Sigma\text{Fe}$ ratio in the illite-like phase can be interpreted as an authentic
361 zonation, from $\sim 55\%$ in crystal rims (conforming to the spectra presented in Figure 8) to
362 $\sim 85\%$ in several crystal core clusters. In the same way, the $\text{Fe}^{3+}/\Sigma\text{Fe}$ ratio distribution draws a
363 subtle zonation in the chlorite, with a $\text{Fe}^{3+}/\Sigma\text{Fe}$ ratio ranging from 18 to $\sim 23\%$ on the crystal
364 rim, in accordance with the spectra shown in Figure 8. Such variations of the $\text{Fe}^{3+}/\Sigma\text{Fe}$ ratio
365 within the crystals are equivalent to several degrees or tens of degrees in the temperature
366 estimation, especially when this variation is associated with a variation in composition. One
367 can expect that this zonation is a crucial issue in application of geothermometers (de Andrade
368 et al. 2006; Bourdelle et al. 2013a), and the redox gap between illite and chlorite raises the
369 issue of the crystallisation processes.

370 In summary, the STXM-based XANES study of FIB foils from the Glarus,
371 Switzerland samples enables (i) estimation of the $\text{Fe}^{3+}/\Sigma\text{Fe}$ ratio in each phase preserving the
372 mineral texture, and (ii) establishment of iron redox mapping with high spatial resolution.

373

374 **Conclusion**

375

376 In this study, we have demonstrated the reliability of two methods that allow
377 quantitative determination of $\text{Fe}^{3+}/\Sigma\text{Fe}$ ratios in silicate phases using STXM coupled with
378 XANES spectroscopy at the Fe $L_{2,3}$ -edges. These approaches are similar to those proposed by
379 van Aken and Liebscher (2002) for EELS measurements but are here calibrated for STXM.
380 The two calibrations are based on reference samples with variable but known $\text{Fe}^{3+}/\Sigma\text{Fe}$ ratios,
381 which were prepared as powders or as FIB foils. We tested these calibrations on three FIB
382 foils extracted from field samples of phyllosilicates (Glarus, Switzerland chlorite and illite
383 samples from metapelites), demonstrating the potential of these methods for quantifying
384 $\text{Fe}^{3+}/\Sigma\text{Fe}$ ratios at the submicrometer-scale. This approach will allow more quantitative
385 mineralogical or geomicrobiological studies requiring estimation of the iron redox state at the
386 nanoscale for terrestrial or extraterrestrial Fe-rich samples.

387

388 **Acknowledgements**

389

390 We are most grateful to the Lawrence Berkeley National Lab and especially to Tolek
391 Tyliczszak for his scientific support, and the Paul Scherrer Institute, Swiss Light Source. We
392 would like to thank the materials characterization department of IFP Energies nouvelles-Lyon
393 and the laboratory of CP2M-Université Aix-Marseille, for technical advice. Thanks are also
394 extended to Nicolas Menguy for his scientific help, and to Christian Chopin (ENS, Paris),
395 Daniel Beaufort (IC2MP, Poitiers), Patricia Patrier (IC2MP, Poitiers) and the Muséum
396 National d'Histoire Naturelle. This study was supported by a grant from the Simone and Cino
397 del Duca Foundation.

398

399 **References**

400

401 Bajt S, Sutton SR, Delaney JS (1994) X-ray microprobe analysis of iron oxidation-states in
402 silicates and oxides using X-ray-absorption near-edge structure (XANES). *Geochim*
403 *Cosmochim Acta* 58 (23):5209-5214

404 Beaufort D, Patrier P, Meunier A, Ottaviani MM (1992) Chemical variations in assemblages
405 including epidote and/or chlorite in the fossil hydrothermal system of Saint Martin (Lesser
406 Antilles). *J Volcanol Geoth Res* 51:95-114

407 Benzerara K, Miot J, Morin G, Ona-Nguema G, Skouri-Panet F, Ferard C (2011)
408 Significance, mechanisms and environmental implications of microbial biomineralization. *C*
409 *R Geosci* 343 (2-3):160-167

410 Benzerara K, Menguy N, Obst M, Stolarski J, Mazur M, Tylicszak T, Brown, Jr., GE,
411 Meibom A (2011) Study of the Crystallographic Architecture of Corals at the Nanoscale by
412 Scanning Transmission X-ray Microscopy and Transmission Electron Microscopy.
413 *Ultramicroscopy* 111 (8): 1268-1275 Bernard S, Benzerara K, Beyssac O, Brown, Jr., GE
414 (2010) Multiscale characterization of pyritized plant tissues in blueschist facies
415 metamorphic rocks. *Geochim Cosmochim Acta* 74 (17):5054-5068

416 Berry AJ, O'Neill HS, Jayasuriya KD, Campbell SJ, Foran GJ (2003) XANES calibrations for
417 the oxidation state of iron in a silicate glass 88 (7):967-977

418 Berry AJ, Yaxley GM, Woodland AB, Foran GJ (2010) A XANES calibration for
419 determining the oxidation state of iron in mantle garnet. *Chem Geol* 278 (1-2):31-37

420 Bluhm, H., Andersson, K., Araki, T., Benzerara, K., Brown, J.G.E., Dynes, J.J., Ghosal, S.,
421 Gilles, M.K., Hansen, H.C., Hemminger, J.C., Hitchcock, A.P., Ketteler, G., Kilcoyne,
422 A.L.D., Kneedler, E., Lawrence, J.R., Leppard, G.G., Majzlam, J., Mun, B.S., Myneni,
423 S.C.B., Nilsson, A., Ogasawara, H., Ogletree, D.F., Pecher, K., Salmeron, M., Shuh, D.K.,
424 Tonner, B., Tylicszak, T., Warwick, T. Yoon, T.H., 2006. Soft X-ray microscopy and
425 spectroscopy at the molecular environmental science beamline at the advanced light source.
426 *J Electron Spectrosc* 150:86-104

427 Bolfan-Casanova N, Munoz M, McCammon C, Deloule E, Ferot A, Demouchy S, France L,
428 Andrault D, Pascarelli S (2012) Ferric iron and water incorporation in wadsleyite under
429 hydrous and oxidizing conditions: A XANES, Mossbauer, and SIMS study. *Am Mineral* 97
430 (8-9):1483-1493

431 Boulard E, Menguy N, Auzende AL, Benzerara K, Bureau H, Antonangeli D, Corgne A,
432 Morard G, Siebert J, Perrillat JP, Guyot F, Fiquet G (2012) Experimental investigation of
433 the stability of Fe-rich carbonates in the lower mantle. *J Geophys Res-Solid Earth* 117

434 Bourdelle F, Parra T, Beyssac O, Chopin C, Moreau F (2012) Ultrathin section preparation of
435 phyllosilicates by Focused Ion Beam milling for quantitative analysis by TEM-EDX. *Appl*
436 *Clay Sci* 59-60:121-130

437 Bourdelle F, Parra T, Beyssac O, Chopin C, Vidal O (2013a) Clay minerals as geo-
438 thermometer: A comparative study based on high-spatial-resolution analyses of illite and
439 chlorite in Gulf Coast sandstones (Texas, USA). *Am Mineral* 98 (5-6):914-926
440 Bourdelle F, Parra T, Chopin C, Beyssac O (2013b) A new chlorite geothermometer for
441 diagenetic to low-grade metamorphic conditions. *Contrib Mineral Petr* 165:723-735
442 Brotton SJ, Shapiro R, van der Laan G, Guo J, Glans PA, Ajello JM (2007) Valence state
443 fossils in Proterozoic stromatolites by L-edge X-ray absorption spectroscopy. *J Geophys*
444 *Res-Biogeosci* 112 (G3)
445 Carlut J, Benzerara K, Horen H, Menguy N, Janots D, Findling N, Addad A, Machouk I
446 (2010) Microscopy study of biologically mediated alteration of natural mid-oceanic ridge
447 basalts and magnetic implications. *J Geophys Res-Biogeosci* 115
448 Chen CT, Idzerda YU, Lin HJ, Smith NV, Meigs G, Chaban E, Ho GH, Pellegrin E, Sette F
449 (1995) Experimental Confirmation of the X-Ray Magnetic Circular-Dichroism Sum-Rules
450 for Iron and Cobalt. *Phys Rev Lett* 75 (1):152-155
451 Cressey G, Henderson CMB, Vanderlaan G (1993) Use of L-edge X-Ray-Absorption
452 Spectroscopy to Characterize Multiple Valence States of 3d Transition-Metals - a New
453 Probe for Mineralogical and Geochemical Research. *Phys Chem Miner* 20 (2):111-119
454 Crocombette JP, Pollak M, Jollet F, Thromat N, Gautiersoyer M (1995) X-Ray-Absorption
455 Spectroscopy at the Fe L(2,3) Threshold in Iron-Oxides. *Phys Rev B* 52 (5):3143-3150
456 de Andrade V, Vidal O, Lewin E, O'Brien P, Agard P (2006) Quantification of electron
457 microprobe compositional maps of rock thin sections: an optimized method and examples. *J*
458 *Metamorph Geol* 24 (7):655-668
459 de Groot FMF, de Smit E, van Schooneveld MM, Aramburo LR, Weckhuysen BM (2010) In-
460 situ Scanning Transmission X-Ray Microscopy of Catalytic Solids and Related
461 Nanomaterials. *ChemPhysChem* 11 (5):951-962
462 de Smit E, Swart I, Creemer JF, Hoveling GH, Gilles MK, Tyliczszak T, Kooyman PJ,
463 Zandbergen HW, Morin C, Weckhuysen BM, de Groot FMF (2008) Nanoscale chemical
464 imaging of a working catalyst by scanning transmission X-ray microscopy. *Nature* 456
465 (7219):222-U239
466 Fialin M, Bézos A, Wagner C, Magnien V, Humler E (2004) Quantitative electron
467 microprobe analysis of Fe³⁺/ΣFe: Basic concepts and experimental protocol for glasses. *Am*
468 *Mineral* 89 (4):654-662
469 Garvie LA, Zega TJ, Rez P, Buseck PR (2004) Nanometer-scale measurements of Fe³⁺/ΣFe
470 by electron energy-loss spectroscopy: A cautionary note. *Am Mineral* 89 (11-12):1610-1616

471 Hanhan S, Smith AM, Obst M, Hitchcock AP (2009) Optimization of analysis of soft X-ray
472 spectromicroscopy at the Ca 2p edge. *J Electron Spectrosc* 173 (1):44-49

473 Heaney PJ, Vicenzi EP, Giannuzzi LA, Livi KJT (2001) Focused ion beam milling: A method
474 of site-specific sample extraction for microanalysis of Earth and planetary materials. *Am*
475 *Mineral* 86 (9):1094-1099

476 Heijboer WM, Battiston AA, Knop-Gericke A, Havecker M, Mayer R, Bluhm H, Schlogl R,
477 Weckhuysen BM, Koningsberger DC, de Groot FMF (2003) In-situ soft X-ray absorption of
478 over-exchanged Fe/ZSM5. *J Phys Chem B* 107 (47):13069-13075

479 Hitchcock AP (2012) aXis 2000 Analysis of X-ray Images and Spectra. McMaster University,
480 Hamilton, ON, Canada

481 Inoue A, Meunier A, Patrier-Mas P, Rigault C, Beaufort D, Vieillard P (2009) Application of
482 chemical geothermometry to lowtemperature trioctahedral chlorites. *Clay Clay Miner*
483 *57(3):371–382*

484 Joswig W, Amthauer G, Takeuchi Y (1986) Neutron-diffraction and Mössbauer spectroscopic
485 study of clintonite (xanthophyllite). *Am Mineral* 71:1194-1197

486 Keeling JL, Raven MD, Gates WP (2000) Geology and characterization of two hydrothermal
487 nontronites from weathered metamorphic rocks at the Uley Graphite Mine, South Australia.
488 *Clay Clay Miner* 48 (5):537-548

489 Lahfid A, Beyssac O, Deville E, Negro F, Chopin C, Goffe B (2010) Evolution of the Raman
490 spectrum of carbonaceous material in low-grade metasediments of the Glarus Alps
491 (Switzerland). *Terra Nova* 22 (5):354-360

492 Lam KP, Hitchcock AP, Obst M, Lawrence JR, Swerhone GDW, Leppard GG, Tyliczszak T,
493 Karunakaran C, Wang J, Kaznatcheev K, Bazylnski DA, Lins U (2010) Characterizing
494 magnetism of individual magnetosomes by X-ray magnetic circular dichroism in a scanning
495 transmission X-ray microscope. *Chem Geol* 270 (1-4):110-116

496 Lauterbach S, McCammon CA, van Aken P, Langenhorst F, Seifert F (2000) Mossbauer and
497 ELNES spectroscopy of (Mg,Fe)(Si,Al)O₃ perovskite: a highly oxidised component of the
498 lower mantle. *Contrib Mineral Petr* 138 (1):17-26

499 Magnien V, Neuville DR, Cormier L, Mysen BO, Briois V, Belin S, Pinet O, Richet P (2004)
500 Kinetics of iron oxidation in silicate melts: a preliminary XANES study. *Chem Geol* 213 (1-
501 3):253-263

502 Miot J, Benzerara K, Morin G, Kappler A, Bernard S, Obst M, Ferard C, Skouri-Panet F,
503 Guigner JM, Posth N, Galvez M, Brown, Jr., GE, Guyot F (2009) Iron biomineralization by
504 anaerobic neutrophilic iron-oxidizing bacteria. *Geochim Cosmochim Ac* 73 (3):696-711

505 Miot J, Maclellan K, Benzerara K, Boisset N (2011) Preservation of protein globules and
506 peptidoglycan in the mineralized cell wall of nitrate-reducing, iron(II)-oxidizing bacteria: a
507 cryo-electron microscopy study. *Geobiology* 9 (6):459-470

508 Munoz M, De Andrade V, Vidal O, Lewin E, Pascarelli S, Susini J (2006) Redox and
509 speciation micromapping using dispersive X-ray absorption spectroscopy: Application to
510 iron chlorite mineral of a metamorphic rock thin section. *Geochem Geophys Geosyst* 7

511 Raabe, J., Tzvetkov, G., Flechsig, U., Böge, M., Jaggi, A., Sarafimov, B., Vernooij, M.G.C.,
512 Huthwelker, T., Ade, H., Kilcoyne, D., Tyliszczak, T., Fink, R.H. Quitmann, C., 2008.
513 PolLux: A new facility for soft X-ray spectromicroscopy at the Swiss Light Source. *Rev Sci*
514 *Instrum* 79

515 Raeburn SP, Ilton ES, Veblen DR (1997a) Quantitative determination of the oxidation state of
516 iron in biotite using X-ray photoelectron spectroscopy: I. Calibration. *Geochim Cosmochim*
517 *Ac* 61 (21):4519-4530

518 Raeburn SP, Ilton ES, Veblen DR (1997b) Quantitative determination of the oxidation state of
519 iron in biotite using X-ray photoelectron spectroscopy: II. In situ analyses. *Geochim*
520 *Cosmochim Ac* 61 (21):4531-4537

521 Rigault C (2010) Cristallochimie de Fer dans les chlorites de basse température : implications
522 pour la géothermométrie et la détermination des paléoconditions redox dans les gisements
523 d'Uranium. University of Poitiers, Poitiers

524 Schingaro E, Scordari F, Mesto E, Brigatti MF, Pedrazzi G (2005) Cation-site partitioning in
525 Ti-rich micas from Black Hill (Australia): A multi-technical approach. *Clay Clay Miner* 53
526 (2):179-189

527 Schmid R, Wilke M, Oberhänsli R, Janssens K, Falkenberg G, Franz L, Gaab A (2003)
528 Micro-XANES determination of ferric iron and its application in thermobarometry. *Lithos*
529 70 (3-4):381-392

530 Stagno V, Ojwang DO, McCammon CA, Frost DJ (2013) The oxidation state of the mantle
531 and the extraction of carbon from Earth's interior. *Nature* 493: 84-88

532 van Aken PA, Liebscher B (2002) Quantification of ferrous/ferric ratios in minerals: new
533 evaluation schemes of Fe L-23 electron energy-loss near-edge spectra. *Phys Chem Miner* 29
534 (3):188-200

535 van der Laan G, Kirkman IW (1992) The 2p Absorption-Spectra of 3d Transition-Metal
536 Compounds in Tetrahedral and Octahedral Symmetry. *J Phys-Condens Matter* 4 (16):4189-
537 4204

538 Wasinger EC, de Groot FMF, Hedman B, Hodgson KO, Solomon EI (2003) L-edge X-ray
539 absorption spectroscopy of non-heme iron sites: Experimental determination of differential
540 orbital covalency. *J Am Chem Soc* 125 (42):12894-12906
541 Waychunas GA, Apter MJ, Brown, Jr., GE (1983) X-ray K-edge absorption spectra of Fe
542 minerals and model compounds: Near-edge structure. *Phy Chem Min* 10 (1):1-9
543 Wilke M, Farges F, Petit PE, Brown, Jr., GE, Martin F (2001) Oxidation state and
544 coordination of Fe in minerals: An FeK-XANES spectroscopic study. *Am Mineral* 86 (5-
545 6):714-730
546 Wilke M, Hahn O, Woodland AB, Rickers K (2009) The oxidation state of iron determined
547 by Fe K-edge XANES-application to iron gall ink in historical manuscripts. *J Anal Atom*
548 *Spectrom* 24 (10):1364-1372

549

550 Tables

551

552 **Table 1** Reference samples used for XANES - $\text{Fe}^{3+}/\Sigma\text{Fe}$ ratio quantification

553

Type	Sample	Source	FeO %wt.*	$\text{Fe}^{3+}/\Sigma\text{Fe}$ Redox ratio	Position of maximum peak intensity (eV)			
					L ₃ -a	L ₃ -b	L ₂ -a	L ₂ -b
Silicate glass	PyrNa	Magnien et al. (2004)	12.83	0.73 ±0.03	708.57	710.04	721.68	723.54
Silicate glass	PyrNa17R	Magnien et al. (2004)	12.75	0.09 ±0.01	708.36	710.77	721.37	723.54
Silicate glass	PyrNa5R	Magnien et al. (2004)	12.92	0.61 ±0.01	708.57	710.04	721.68	723.54
Silicate glass	PyrNa750	Magnien et al. (2004)	12.68	0.94 ±0.03	708.67	710.25	721.68	723.54
Silicate glass	PyrNa1200	Magnien et al. (2004)	13.52	0.89 ±0.05	708.67	708.93	721.84	724.54
Nesosilicate	Fayalite	Neuvillle D.	70.50	0.00 ±0.00 [‡]	708.09	710.71	720.75	723.54
Phyllosilicate	Smectite Nau-2	Keeling et al. (2000)	34.10	1.00 ±0.00 [‡]	708.57	710.35	721.84	723.54
Phyllosilicate	Clintonite	Joswig et al. (1986)	3.01	0.69 ±0.03 [‡]	708.25	710.08	721.49	723.53
Phyllosilicate	Ti-mica	Shingaro et al. (2005)	19.38	0.03 ±0.03 [‡]	708.04	710.04	721.00	723.54
Phyllosilicate	Chlorite 'Prochlorite'	MNHN [†]	14.50	0.30 ±0.10 [‡]	708.26	710.21	721.51	723.51
Phyllosilicate	Chlorite Ch1	This study	40.10	0.17 ±0.05	708.04	710.19	721.00	723.54
Phyllosilicate	Chlorite GAB 42	Rigault (2010)	28.50	0.14 ±0.03	708.15	710.46	720.75	723.54
Phyllosilicate	Chlorite VNI 92	Rigault (2010)	20.73	0.35 ±0.03	708.15	710.25	720.75	723.54
Phyllosilicate	Chlorite VNI 114	Rigault (2010)	20.82	0.20 ±0.03	708.04	710.25	720.75	723.54

554 * $\Sigma\text{Oxides wt}\% = 100$ as basis and all iron reported as ferrous. [†] MNHN: Collection of Muséum National

555 d'Histoire Naturelle, France. [‡] assumed error deviation.

556

557 **Table 2** AEM chemical representative analyses of Glarus chlorites and comparison of
 558 thermometers results taking into account $\text{Fe}^{3+}/\Sigma\text{Fe}$ ratios (Eq. (3)); regarding the scatter of
 559 data on Figure 3, we infer a precision of $\pm 5\%$ on the $\text{Fe}^{3+}/\Sigma\text{Fe}$. Analyses were carried out on
 560 crystal rims, along the illite-chlorite contact, according to Bourdelle et al. (2013a).
 561 Temperature estimations were performed with Bourdelle et al. (2013b) and Inoue et al. (2009)
 562 thermometers, with and without consideration of Fe^{3+} , in accordance with the
 563 recommendations made by each authors. Taking into account the $\text{Fe}^{3+}/\Sigma\text{Fe}$ ratios in the Inoue
 564 model allows to obtain similar results to those calculated with the Bourdelle model (which is
 565 a pure Fe^{2+} model), i.e., with a difference less than 30°C (equivalent to the uncertainty of each
 566 model)
 567

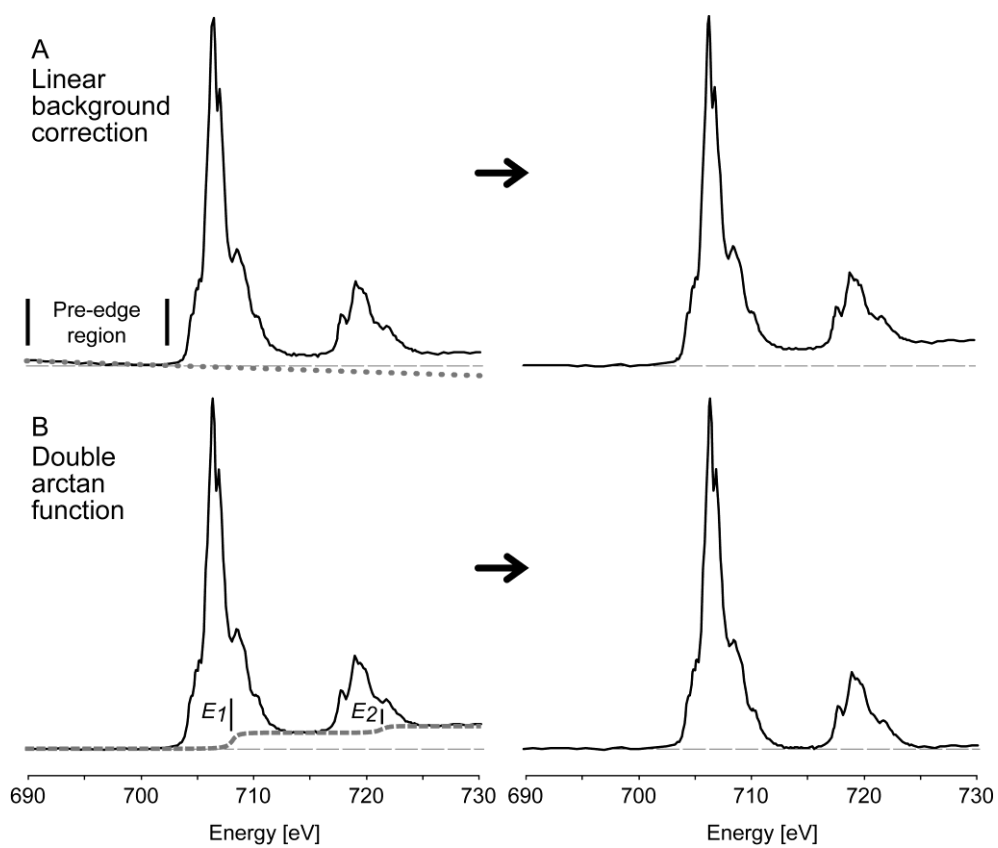
Chlorite [%wt]	GL07 13	GL07 20	GL07 16
SiO_2	32.70	31.40	31.57
TiO_2	0.07	0.06	0.04
Al_2O_3	26.41	25.56	26.02
FeO	26.63	28.53	25.13
MnO	0.00	0.00	0.00
MgO	13.75	13.97	16.70
CaO	0.06	0.10	0.29
Na_2O	0.00	0.04	0.00
K_2O	0.39	0.35	0.25
$\text{Fe}^{3+}/\Sigma\text{Fe}$ [%]	22.30	23.80	27.90
$T_{\text{BOU}} [^\circ\text{C}]$	135	170	182
$T_{\text{INO-Fe}^{2+}} [^\circ\text{C}]$	165 (+30)	236 (+66)	258 (+76)
$T_{\text{INO-Fe}^{3+}} [^\circ\text{C}]$	145 (+10)	196 (+26)	210 (+28)

568 T_{BOU} : temperatures calculated with the Fe^{2+} -pure model of Bourdelle et al. (2013b), considering $\text{Fe}_{\text{tot}} = \text{Fe}^{2+}$.
 569 $T_{\text{INO-Fe}^{2+}}$: temperatures calculated with the Inoue et al. (2009) model, considering $\text{Fe}_{\text{tot}} = \text{Fe}^{2+}$. $T_{\text{INO-Fe}^{3+}}$:
 570 temperatures calculated with the Inoue et al. (2009) model, using the estimated $\text{Fe}^{3+}/\Sigma\text{Fe}$.

571

572 **Figures**

573

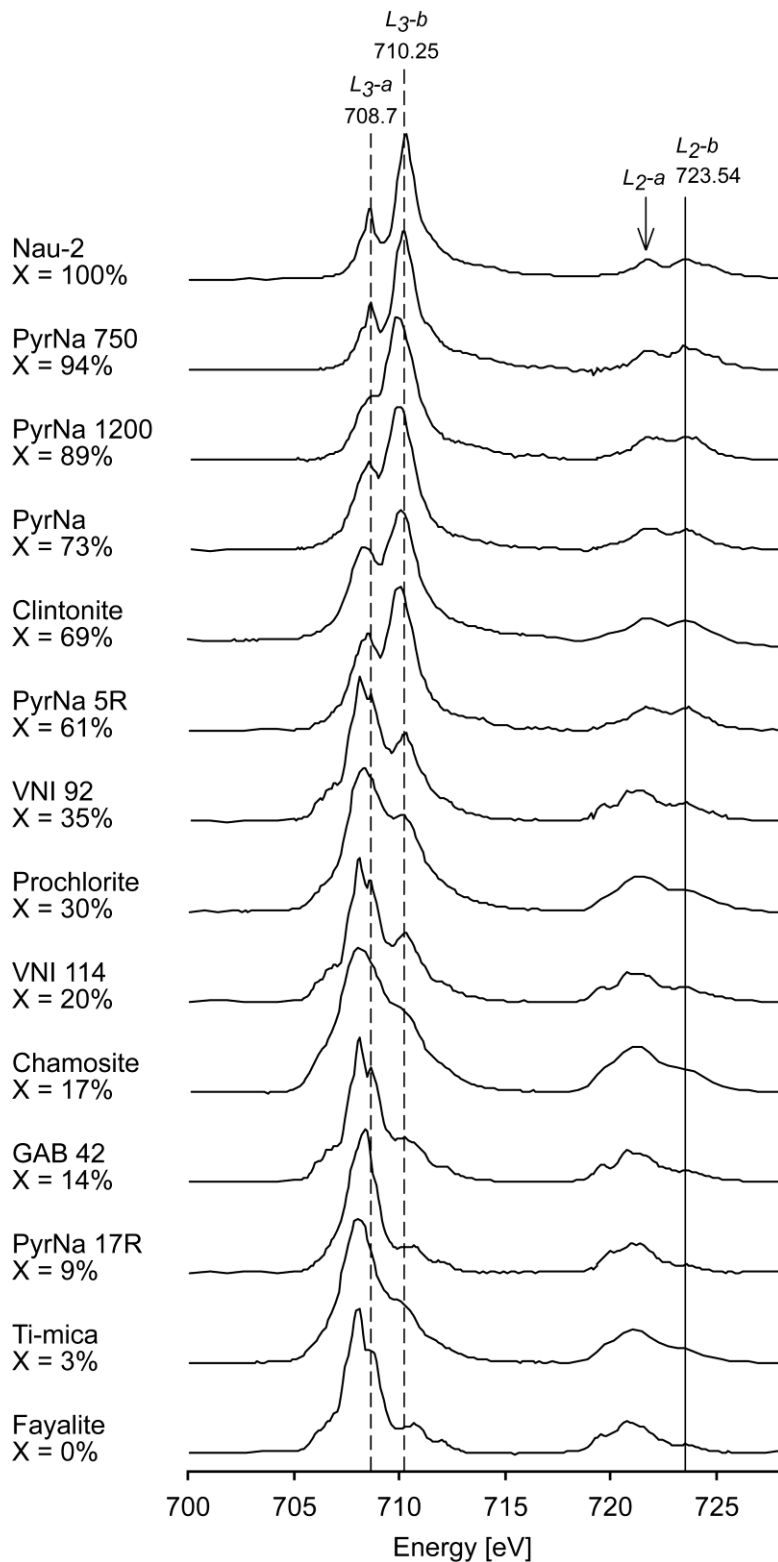


574

575 **Fig. 1** Subtraction of background from XANES spectra at Fe L-edge, using linear and double

576 arctan functions ($w_1 = w_2 = 1$ eV), for chlorite GAB 42

577

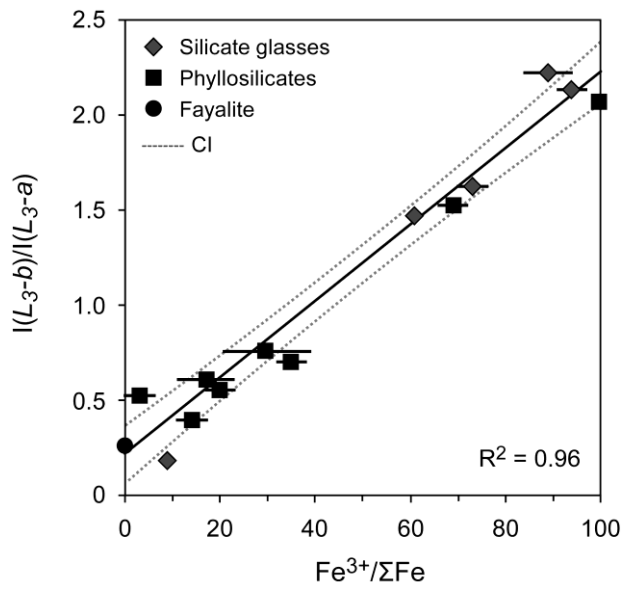


578

579 **Fig. 2** Representative XANES spectra at the Fe L_{2,3}-edges for the reference silicates. The
 580 spectra have been normalised to the integral Fe L₃-edge intensity, and some of the spectra
 581 have been shifted vertically for clarity (normalized intensity with arbitrary units). The dotted
 582 lines represent the energies fixed to determine the Fe³⁺ concentration from the Fe L₃-peaks'

583 intensity ratio. The solid line underlines the position of L_{2-b} maximum intensity, which is
584 identical for all spectra. $X = Fe^{3+}/\Sigma Fe$ ratios of Table 1

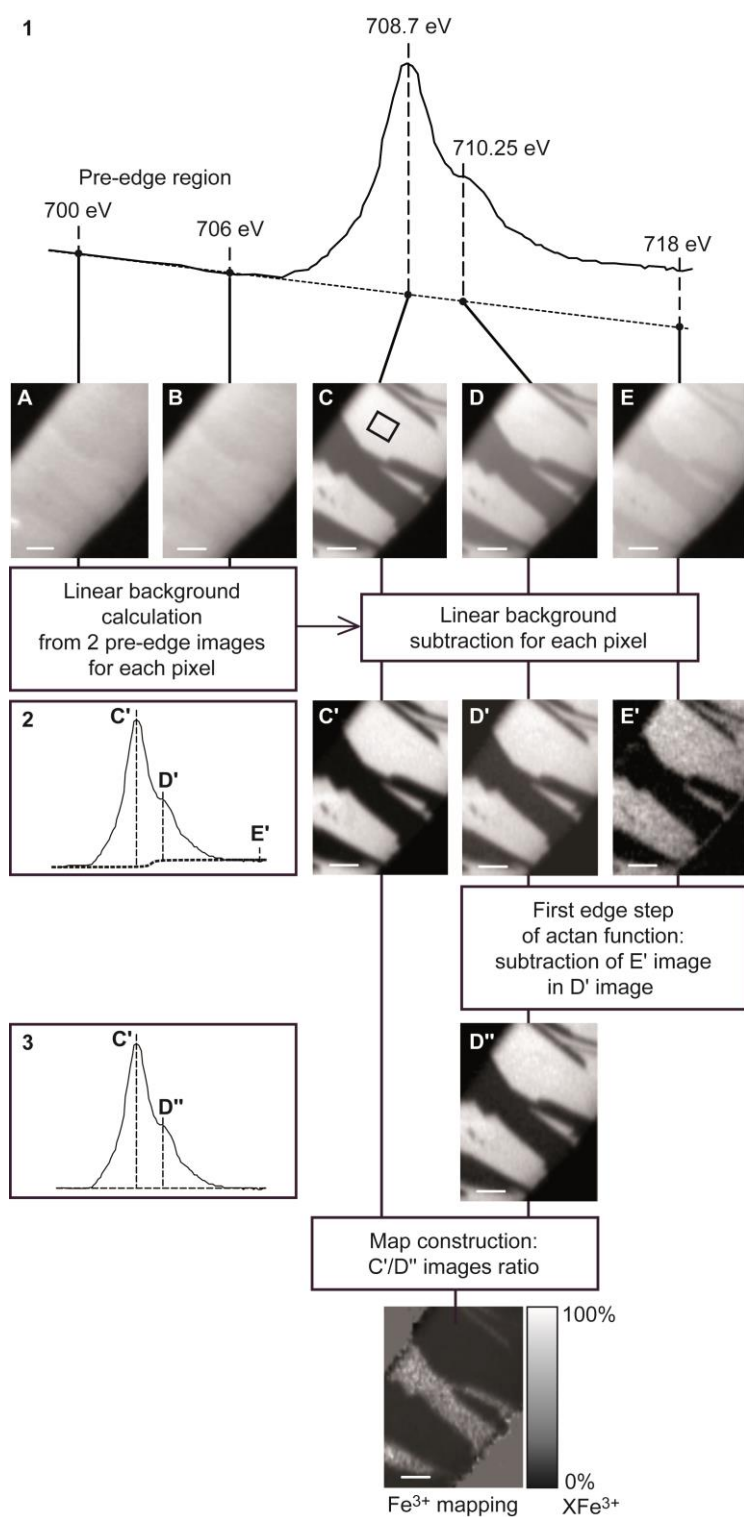
585



586

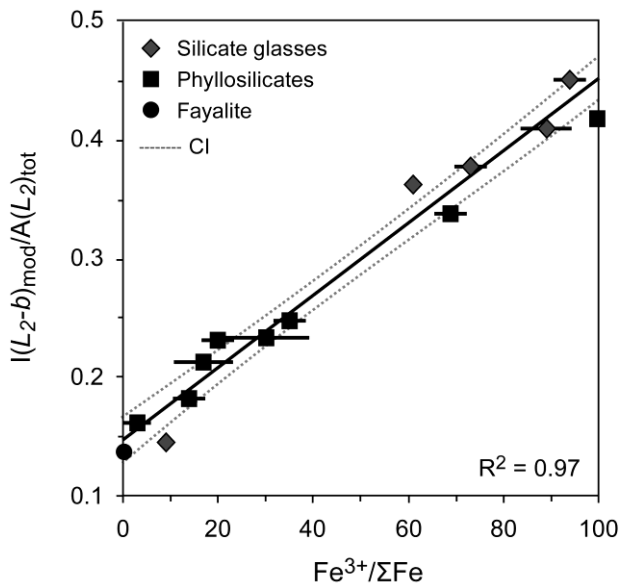
587 **Fig. 3** L_{3} -edge intensity ratio $I(L_{3-b})/I(L_{3-a})$ from XANES spectra versus ferric iron
588 concentration $Fe^{3+}/\Sigma Fe$ quantified by independent methods for the selected silicates. CI:
589 confidence interval (95%)

590

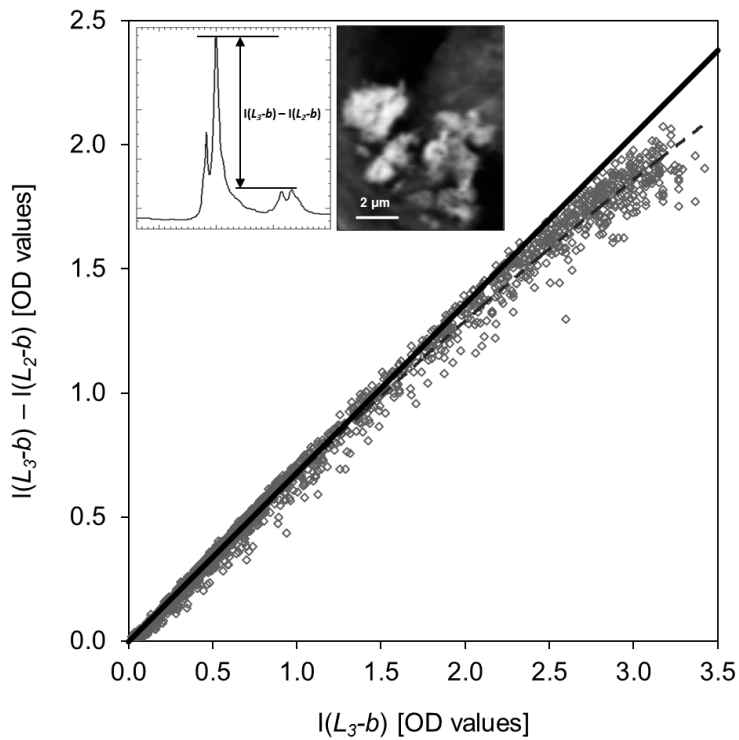


591
 592 **Fig. 4** Determination of the $\text{Fe}^{3+}/\Sigma\text{Fe}$ ratio from 5 selected energy images: two images in the
 593 pre-edge (to apply the “linear background correction” at each pixel of the image), one at 708.7
 594 eV to quantify the L_3 -a peak, one at 710.25 eV to quantify the L_3 -b peak, and one at 718 eV,
 595 to remove the edge step of the arctan function. Finally, the ratio of the resulting 708.7 and
 596 710.25 eV images can be used to determine the R_{L_3} parameter at each pixel of the image, and
 597 obtain iron redox mapping. All images are OD images (70 x 90 pixels), where the illite and

598 chlorite are the dark- and light- grey phases, respectively. As an illustration, spectrum #1 was
 599 retrieved from 110 images (i.e., 110 energy points) on a chlorite area (dark rectangle on image
 600 C); spectrum #2 was obtained after the linear function subtraction from spectrum #1 and
 601 spectrum #3 after the actan function subtraction from spectrum #2. Case of FIB foil of Glarus
 602 GL07 20 sample.
 603



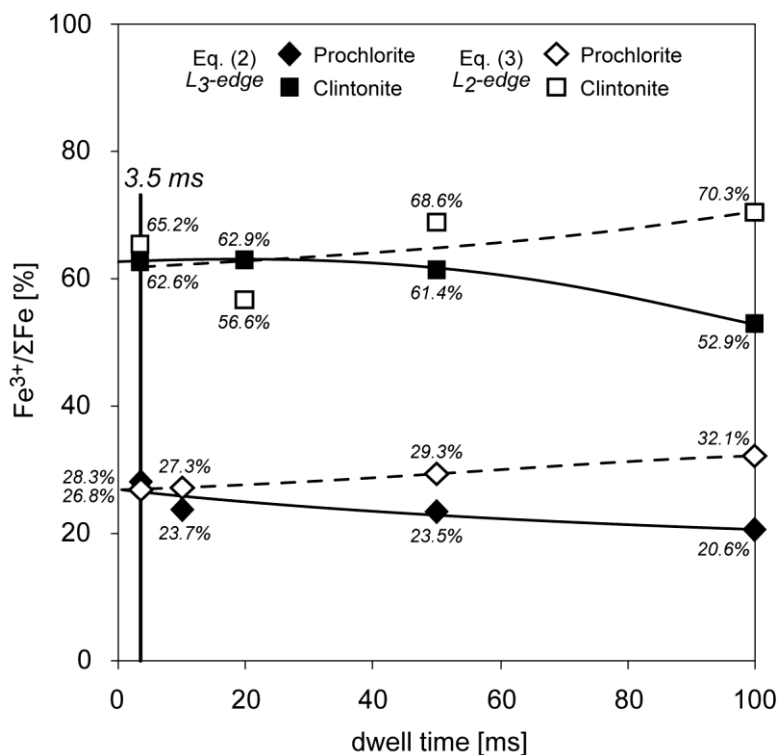
604
 605 **Fig. 5** L_2 -edge integral intensity ratio (i.e., integral intensity of maximum L_2 -b ± 0.1 eV over
 606 total integral intensity (area) of L_2 -edge) from XANES spectra versus ferric iron
 607 concentration $Fe^{3+}/\Sigma Fe$ quantified by independent methods for the reference silicates. CI:
 608 confidence interval (95%)
 609



610

611 **Fig. 6** Difference, pixel by pixel, of intensity detected between the 710.25 and the 723.54 eV
 612 images (in which a pre-edge image was not subtracted) versus the intensity of the 710.25 eV
 613 image of a Smectite Nau-2 STXM-map (Nau-2, 72 x 88 pixels = 6336 points), i.e., the L_3 -b –
 614 L_2 -b intensity difference versus the L_3 -b intensity for each pixel. The dashed line was
 615 calculated from a quadratic equation. Insets: representative spectra and optical density image
 616 (710.25 eV) for Nau-2 sample

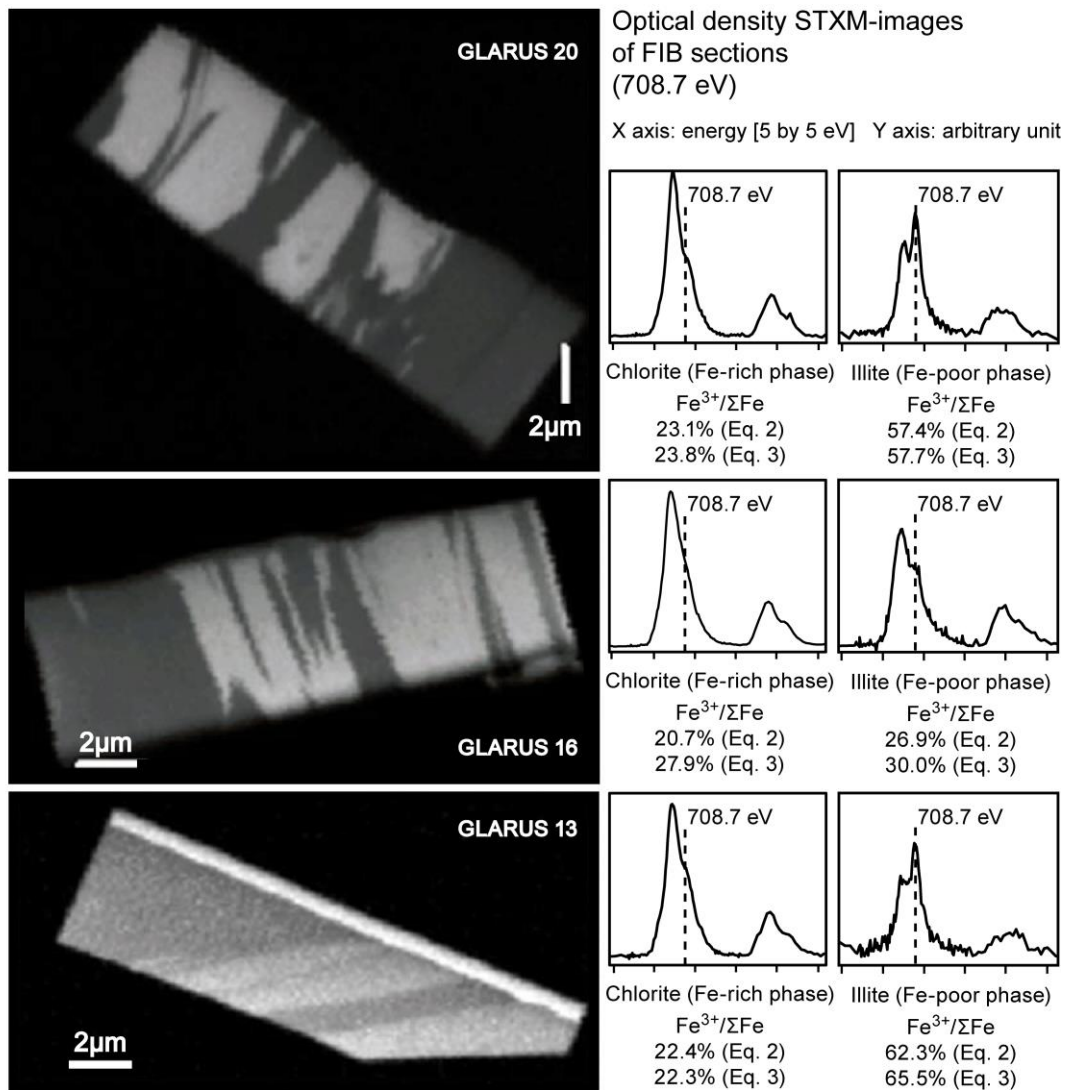
617



618

619 **Fig. 7** Beam-induced radiation damage during STXM analyses of chlorite ‘prochlorite’
 620 ($XFe^{3+} = 30\%$) and clintonite ($XFe^{3+} = 69\%$). Evolution of the $Fe^{3+}/\Sigma Fe$ ratios as a function of
 621 dwell time, estimated by Eq. (2) and (3) from XANES spectra. Data were fit by a quadratic
 622 function. The beam radiations (increasing dwell) involve (1) a decrease of XFe^{3+} calculated
 623 from L_3 -edge (Eq. 2) and (2) an increase of XFe^{3+} calculated from L_2 -edge (Eq. 3). Spectra of
 624 reference samples and Glarus samples (see text) were recorded with a dwell time of 1.3-
 625 3.5 ms per point and energy: the beam radiation damage is thus negligible with our analytical
 626 conditions for data collection

627



628

629

630

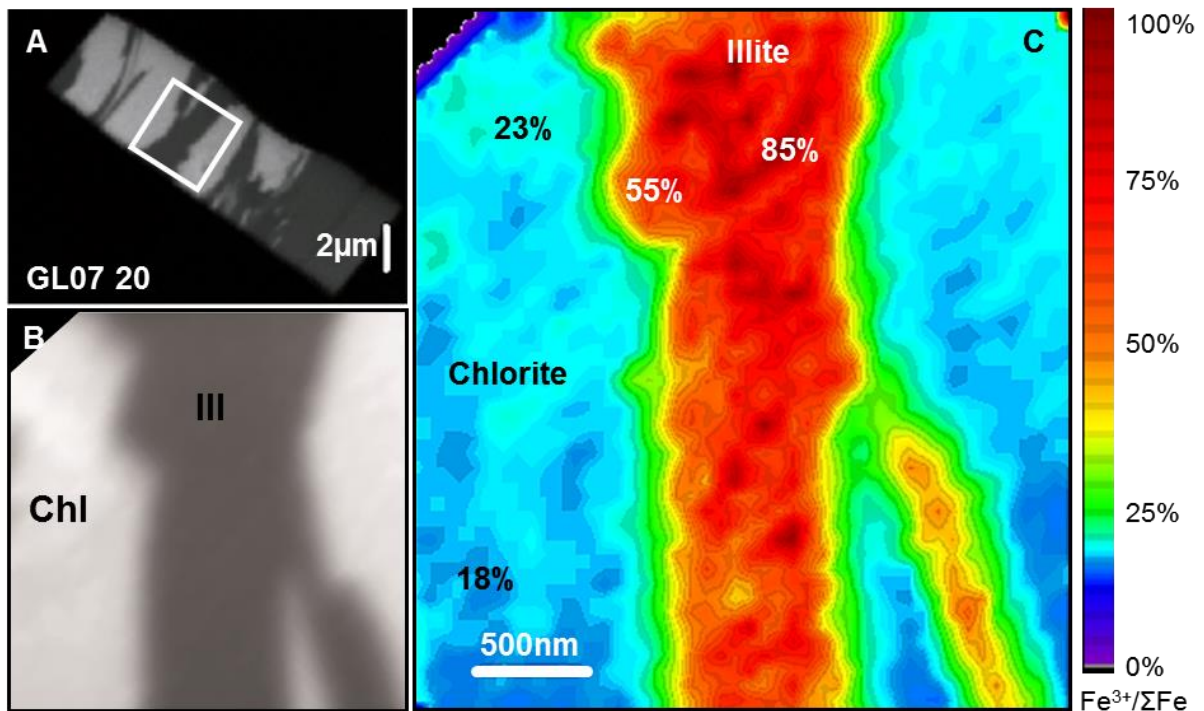
631

632

633

634

Fig. 8 Scanning transmission x-ray microscopy (STXM) and XANES analysis and Fe³⁺/ΣFe estimations for FIB foils of Glarus samples (chlorite and illite). [Left] Optical density images of FIB foils at 708.7 eV. The illite and chlorite are the dark- and light- grey phases, respectively. [Right] XANES spectra of areas of interest and calculated Fe³⁺ concentrations associated (crystals rims)



635

636 **Fig. 9** Quantitative Fe redox nanomapping on FIB foil of Glarus GL07 20 sample. (a) Optical
 637 density image at 708.7 eV of Glarus GL07 20 FIB section, where the illite and chlorite are the
 638 dark- and light- grey phases, respectively. (b) Optical density image at 708.7 eV of the area of
 639 interest. (c) iron redox mapping, calculated from the 708.7 to 710.25 eV images ratio coupled
 640 with Eq. (2). The illite-chlorite contacts were analysed by AEM to check that they are
 641 approximately perpendicular to the FIB foil surface, i.e., there is only a small overlap between
 642 the two minerals at their contact. The spatial averaging effect of the x-ray beam over the pixel
 643 size (i.e., 88 nm) sets the limit of the minimum distance over which illite-chlorite contacts can
 644 be discriminated. Beyond this distance, the intracrystalline variation of $\text{Fe}^{3+}/\Sigma\text{Fe}$ ratio in the
 645 illite-like phase can be interpreted as an authentic zonation, from 55% to 85% in several
 646 crystal core clusters

647

648

649

650